Phase Separation in Polyfluorene-Based Conjugated Polymer Blends: Lateral and Vertical Analysis of Blend Spin-Cast Thin Films

Ji-Seon Kim,*,†,‡ Peter K. H. Ho,†,‡ Craig E. Murphy,‡ and Richard H. Friend†,‡

Cavendish Laboratory, Madingley Road, Cambridge CB3 0HE, UK, and Cambridge Display Technology Ltd., Madingley Road, Cambridge CB3 0TX, UK

Received November 21, 2003; Revised Manuscript Received February 17, 2004

ABSTRACT: We have studied phase separation in polyfluorene-based electroluminescent polymer blends consisting of poly(2,7-(9,9-di-*n*-octylfluorene-*alt*-benzothiadiazole) (F8BT) and poly(2,7-(9,9-di-*n*-octylfluorene)-*alt*-(1,4-phenylene-((4-*sec*-butylphenyl)imino)-1,4-phenylene)) (TFB). We present detailed studies on spin-cast thin-film morphology of the blends, using micro-Raman spectroscopy and X-ray photoelectron spectroscopy. Micron-scale lateral phase separation is observed in these blend thin films. However, these phase-separated domains are not pure at the submicron length scale, and a nanoscale vertical phase segregation occurs with enrichment of the lower surface energy component (TFB) at both air and substrate interfaces. Imaging of the spatial uniformity of electroluminescence emission on the microscopic scale indicates spatially localised charge-carrier recombination in light-emitting diodes (LEDs) fabricated with these blends. On the basis of these studies, we propose a model for the development of thin-film phase-separated structure in spin-cast F8BT:TFB blends. LEDs without an additional hole-injection/transporting layer such as a poly(styrenesulfonate)-doped poly(3,4-ethylenedioxythiophene) (PEDT:PSS) have also been characterized to examine the self-organized vertical phase structure found in these blends. The results show that initial performance equivalent to devices with a PEDT:PSS layer is achievable in LEDs which contain only a single layer of F8BT:TFB blend material, confirming that the TFB wetting layer acts efficiently as a hole-accepting/transporting layer.

I. Introduction

Conjugated polymers show interesting semiconductor properties owing to the presence of delocalized electrons in their backbone structure. Light-emitting diodes (LEDs) based on conjugated polymers have received considerable attention after the first report in 1990.[1] These LEDs typically comprise of a polymer thin film sandwiched between a transparent conducting oxide anode such as indium−tin oxide (ITO) and a metal cathode. When a voltage is applied across the diode, charge carriers are injected into the polymer-active layer in which recombination and light emission occur.[2,3] This discovery has spawned immense interest from both commercial and academic laboratories worldwide. This is because of the perceived processing advantages inherent to polymeric semiconductor materials, which could open new applications in novel display, logic, and light-detection systems.

For polymer LEDs, much progress has been made in improving their performance and reliability (brightness, efficiency, and drive voltage).[4−9] The use of electroluminescent polymer blends as an active material has brought a new way to fabricate highly efficient organic devices.[10−19] In particular, polymer LEDs fabricated with poly(2,7-(9,9-di-*n*-octylfluorene-*alt*-benzothiadiazole) (F8BT) blended with poly(2,7-(9,9-di-*n*-octylfluorene)-*alt*-(1,4-phenylene-((4-*sec*-butylphenyl)imino)-1,4-phenylene)) (TFB) as the emissive layer show a significantly improved device performance.[20−22] These state-of-the-art polymer LEDs based on the F8BT:TFB blend produce yellow-green emission with very low threshold voltages for light emission (below 2 V), standard display brightnesses of 100 cd/m^2 at 2.1 V, with efficiencies above 18 lm/W, and very bright operation at higher voltages. These devices have excellent stability under operation (many thousands of hours at room temperature). Interestingly, these highly efficient F8BT:TFB LEDs show considerable structures in electroluminescence (EL) emission at the micron-length scale originated from a phase separation of the two EL polymers in their blends.

Despite their significantly improved device performance, a number of scientific challenges remain to more fully understand, quantify, and predict the behavior of the polymer blend LEDs. For example, the dependence of device performance on the phase separation of EL polymers and the factors affecting the development of phase-separated structures from polymer blend solutions are still poorly understood. To understand the interplay between the polymer blends and polymer blend devices, it is therefore important to consider the chemical nature of the polymers and solvent, since these parameters determine the phase diagram for the solution system and the evolution of the lateral and vertical phase separation and thin-film morphology. The study of polymer phase separation is a very rich field with literature stretching back to the birth of polymers itself.[23−29] However, the amounts of published data on the behavior of conjugated polymers, especially data on ultrathin films (less than 100 nm thick), that are directly relevant to the properties of organic semiconductor devices are scarce.

In this report, we present the detailed studies on the phase separation in polyfluorene-based electroluminescent polymer blends consisting of F8BT and TFB. We

* Corresponding author: e-mail jsk20@cam.ac.uk, Tel 44-(0)-1223-337285, Fax 44-(0)1223-353397.
† Cavendish Laboratory.
‡ Cambridge Display Technology Ltd.

10.1021/ma035750i CCC: $27.50
Published on Web 03/23/2004

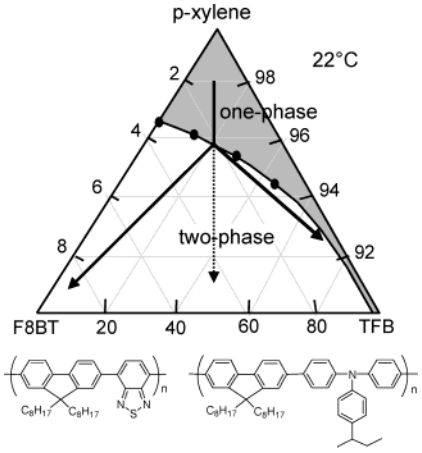

Figure 1. Phase diagram for ternary blend system (F8BT + TFB + *p*-xylene) and the chemical structures of F8BT, poly(2,7-(9,9-di-*n*-octylfluorene)-*alt*-benzothiadiazole), and TFB, poly(2,7-(9,9-di-*n*-octylfluorene)-*alt*-(1,4-phenylene-((4-*sec*-butylphenyl)imino)-1,4-phenylene)).

first discuss the phase diagram of this F8BT-TFB-*p*-xylene ternary blend system, and then the film morphology of the blends, as revealed by micro-Raman spectroscopy and X-ray photoelectron spectroscopy (XPS). From all of these studies, we propose a model for the development of the thin-film phase-separated structures of F8BT:TFB blends. We also characterize F8BT:TFB LEDs with/without an additional hole-injection/transporting layer such as a poly(styrenesulfonate)-doped poly(3,4-ethylenedioxythiophene) (PEDT:PSS) (Bayer) to examine the self-organized vertical phase-separation structure in these blend thin films.

II. Experimental Section

A. F8BT−TFB Polymer Solutions and Thin Films. The EL polymers studied here are F8BT (M_n = 108K, bulk T_g = 118 °C) and TFB (M_n = 56K, bulk T_g = 148 °C). Their chemical structures are shown in Figure 1. F8BT is a high electron mobility polymer,[30,31] and TFB is a high hole mobility polymer.[32] The F8BT and TFB polymer solutions were prepared by dissolving each polymer in mixed xylene to produce a concentration of ∼1.4% w/v (14 mg/mL). For the blends, the F8BT and TFB solutions were mixed to give various blend ratios (by weight) of F8BT:TFB 100:0, 95:5, 75:25, 50:50, 25:75, and 0:100. A ∼80−100 nm thick polymer layer was then spin-coated from these solutions on the top of the quartz or the oxygen-plasma cleaned indium−tin oxide (ITO)−glass substrates (Balzers).[4] For the Raman measurement of the solutions, each blend solution was diluted to have a concentration of <0.1% (w/v) to eliminate possible phase separation in blend solutions.

B. F8BT−TFB LEDs. LEDs were fabricated by using oxygen-plasma-treated ITO as anode,[4] F8BT:TFB blend as an active layer, and Ca as a cathode. For LEDs with additional hole-transporting and injection layer, a ∼60 nm thick PEDT:PSS layer was first spin-coated from a water solution on the top of the ITO substrate and then baked at 200 °C for 10 min in an oven with N_2 flow. An ∼80 nm thick F8BT:TFB (50:50) layer was spin-coated on the top of the PEDT:PSS layer in a glovebox. 2.0 × 7.5 mm devices were completed by evaporating Ca (∼5 nm) with an Al (∼400 nm) protecting layer at a base pressure better than 10^{-6} mbar. Finally, the devices were encapsulated using a cover glass and epoxy resin in the glovebox without exposing to air.

C. Thin-Film Morphology. A commercial atomic force microscope (AFM) in tapping mode (NanoScope II, Digital Instruments Inc.) was used to investigate the morphological features in the polymer blend thin films. Optical microscope was used to take the images of photoluminescence (PL) of the blend thin films under blue excitation and electroluminescence (EL) of the blend LEDs.

D. Micro-Raman Spectroscopy. Samples (polymer solutions or thin films) were excited in a 180° backscattering geometry by a 633 nm HeNe laser (<1 mW) focused through a ×60 (NA = 0.7) cover-glass-corrected objective or a ×50 (NA = 0.7) normal microscope objective in a Renishaw 2000 Raman microscope. Spectra accumulation was done for 100 s. No significant visible laser damage was observed through the microscope even at prolonged exposure. The sample was excited below its optical band edge to avoid the fluorescence background and at a low laser power to reduce the possible photooxidation. The Rayleigh-scattered light was eliminated by two holographic notch filters, and only the Raman-scattered light dispersed by a grating was collected by a Peltier-cooled CCD detector.[22]

E. X-ray Photoelectron Spectroscopy (XPS). Core-level and survey X-ray photoelectron spectra were acquired on a ESCALAB MKII spectrometer at a base pressure better than 10^{-9} mbar using Mg $K\alpha_{1,2}$ X-ray photons (1253.6 eV) irradiating 54.7° relative to electron analyzer entrance. The photoejected electrons were analyzed by a concentric hemispherical analyzer operated at constant pass energy of 20 eV for core-level spectra and 50 eV for survey spectra. The photoemission angle (θ) was set at 90° (normal) and/or 20° (i.e., 70° from normal) by rotating the sample. The X-ray gun was operated at 150 W and emission distributed over an area of about 5 mm diameter on the substrate at θ = 90°.

As the samples were on conducting ITO substrates, sample charging was insignificant and electron flood gun operation was not necessary. To compensate for work function variations and facilitate comparison, the photoelectron binding energies (BE) were given on the chemical binding energy scale and referenced to the C 1s BE defined to be 285.0 eV, as appropriate for C 1s spectra strongly weighted by aliphatic and some aromatic hydrocarbons.[33]

Core-level spectra were processed by linear background subtraction and displayed normalized to the intensity of the specified core levels. For atomic stoichiometries, the integrated intensities were corrected with empirical sensitivity factors taking into account the atomic photoionization cross sections, the electron inelastic mean free path, and the spectrometer intensity−energy response function. The quantification error is expected to be ±10% from systematic effects.

The photoelectron inelastic mean free path (λ_0) in the sample determines the information depth interrogated by the technique. This mean free path value depends on the photoelectron kinetic energy and hence the excitation energy and differs across the binding energy spectrum. However, for the atomic states studied in this report (S 2p, Si 2p, C 1s, N 1s, and O 1s), the variation is small and can be approximated to be nearly constant at ca. 25 Å. At θ = 90°, the photoemission depth is therefore ca. 25 Å, and the information depth is usually taken to be $3\lambda_0$ (i.e., 75 Å).

To analyze the film−air surface, the film with the substrate was directly mounted into the spectrometer. To analyze the film−substrate interface, a duplicate film on ITO was delaminated by attaching the film surface to carbon adhesive tape and gentle pulling just prior to the experiment. Visual examination showed perfect delamination and a smooth resultant film surface. In one case, when a duplicate of the delaminated film was kept overnight in ambient, no significant difference was observed from the film prepared just prior to insertion into the vacuum chamber. This shows that significant evolution of the film surface does not occur on the time scale of hours. This is consistent with the relatively high T_g of the polymers used.

III. Results and Discussion

A. F8BT−TFB−*p*-Xylene Ternary System Phase Diagram. The thermodynamic phase diagram produces

Table 1. Solubility Parameters and Surface Energy (γ) of F8BT, TFB, and *p*-Xylene[a]

material	δ_d $(J/cm^3)^{1/2}$	δ_p $(J/cm^3)^{1/2}$	δ_h $(J/cm^3)^{1/2}$	δ $(J/cm^3)^{1/2}$	γ (mJ/m^2)
F8BT	19.1−21.3	0.10−0.11	3.2−3.4	19.4−21.6	40−45
TFB	17.1−19.1	0.05−0.06	2.7−2.9	17.3−19.3	35−40
p-xylene[b]	16.6−17.3	1.0	1.0	16.7−17.4	28.37

[a] δ_d = van der Waals (or dispersion) component, δ_p = polar component, δ_h = hydrogen-bonding component, and $\delta = (\delta_d^2 + \delta_p^2 + \delta_h^2)^{1/2}$ calculated by the method of Hoftyzer and Van Krevelen.[34] [b] Values from ref 34.

a useful guide for predicting the behavior of the solution during a film-coating process. For a solution with two polymers, a ternary system exists, i.e., polymer biblend plus solvent. We have determined experimentally the phase diagram for the F8BT + TFB + *p*-xylene system at 22 °C (Figure 1). F8BT has only a limited solubility of ∼3.5% in this solvent and forms easily a viscous gel even at low concentrations. TFB, however, is miscible at all compositions, and a viscous gel only appears at compositions beyond ∼40%.

The solubility parameters and surface energies of F8BT, TFB, and *p*-xylene were determined using group contribution methods with the data tables of Hoftyzer and Van Krevelen[34] and an estimate of conjugation contributions (Table 1). The higher cohesive energy of F8BT (40−45 mJ/m^2) relative to TFB (35−40 mJ/m^2) is traced to the presence of highly polarizable BT units and the better interchain stacking of this polymer compared to TFB, which has three phenylene units arranged in a puckered manner. Despite uncertainties in some of the input parameters, the trend is expected to be correct, owing to the sizable difference and the known accuracy of group contribution methods.[34]

The results predict that *p*-xylene will be a better solvent for TFB than for F8BT and that TFB has a lower surface energy than F8BT. Because of this large difference in solubility behavior, the phase diagram is highly skewed, and as the solvent evaporates, an F8BT-rich phase will form at an early stage. This is confirmed by observation of the solution state itself for compositions inside the coexistence curve (evidenced by an "oil and water" appearance). As the solvent fraction reduces, the system will cross the phase boundary and split into two phases, each of which comprises the solvent and F8BT or TFB. (F8BT is the primary polymer in one phase, and TFB is the primary polymer in the other phase.) We will show from compositional analysis here that under spin-casting conditions both of these phases are impure with significant admixture of the minority polymer component.

B. Blend Thin-Film Morphology. Figure 2a−c shows the tapping mode AFM images of the ∼80−100 nm thick spin-cast F8BT:TFB blend films with different blend ratio of F8BT and TFB (75:25, 50:50, and 25:75). As the F8BT:TFB blend ratio is varied, the surface morphology as seen by AFM is altered. For the 75:25 blend, there is a high matrix phase with a lower enclosed phase (lateral size 0.1−0.5 μm), the height difference being ∼10 nm. For the 50:50 blend, the features are much larger (lateral size 2−5 μm) with a height difference of ∼30−50 nm. For the 25:75 blend, the enclosed phase is higher with "volcano crater" appearance, i.e., a high rimmed mesa. These high phases are of 0.5−1.0 μm lateral dimension, the height difference being ∼10−20 nm. It should be also noted that the lateral size of the features is much larger than the average film thickness (∼0.1 μm) and that there are relatively large variations in the height of the film surface (tens of nanometers). These characteristic surface feature sizes are not only composition dependent (polymer and solvent composition) but also processing dependent (temperature, postbake, etc.).

The distribution of phases seen in AFM data is quantitatively examined using the Bearing function. The depth distribution of the AFM scans is bimodal, indicating the presence of two main phases, the higher and the lower phases. By using Gaussian fitting, the projected geometric phase ratio, as seen from the top surface of the film, was calculated (Figure 2d). This gives an AFM "footprint" for the blend films. Note that the projected F8BT fractions are not the same as the original blend contents.

In all cases, the optical microscopy, which allows identification of the F8BT under blue excitation (excitation with blue light results in green luminescence from only F8BT), has confirmed that the higher-lying phase is F8BT or F8BT-rich and lower-lying phase is TFB or TFB-rich (see Figure 3b for the 50:50 blend film). This also confirms that a phase inversion occurs near the middle 50:50 compositions, when interconnected "ridgeline" F8BT or F8BT-rich phases with isolated TFB or TFB-rich pockets invert to give interconnected "valley" TFB or TFB-rich phases with isolated F8BT or F8BT-rich pockets that take on a "cratered" appearance.

For the LED fabricated with the 50:50 F8BT:TFB blend film as an active layer, the PL image which shows a clear micron-length scale phase separation of this blend film is also observed inside the device structure. When the device is turned on, the yellowish-green EL emission which is nonuniform at the micron-length scale (but uniform to the eye) due to phase separation in the polymer blend film is clearly seen (see Figure 2 in ref 20). Comparison with the PL image reveals that the EL emission is predominantly produced at the interfaces between the TFB or TFB-rich (domain i) and F8BT or F8BT-rich (domain ii) phases. This EL image provides evidence that electron−hole recombination takes place preferentially at these domain boundaries between two phases.

C. Lateral Phase Compositions. To determine quantitatively the composition of the materials in different domains of F8BT:TFB thin films, we used Raman microscopy.[35] We have previously demonstrated how micro-Raman spectroscopy could be used to yield new insights into organic device extrinsic and intrinsic degradation through spectroscopic in-situ monitoring of the active layer in working devices.[22,36] Raman microscopy has a number of distinctive advantages over infrared microscopy for the vibrational spectroscopic study of the conjugated polymers.[22,36−38] In particular, conjugated polymers have a large Raman scattering cross section for the phonon modes that are coupled to the $\pi-\pi^*$ electronic excitation which are of most interest in this work. Most importantly, the optical probe used in Raman microscopy can be focused to a far smaller spot (of the order of ∼0.5 μm for λ = 633 nm) than an infrared probe (of the order of 5 μm for λ = 4−10 μm). These unique capabilities enable us to carry out the chemical and compositional analyses of the polymer blend thin films.

Figure 4 shows the normalized Raman spectra of ∼100 nm thick neat F8BT (a) and TFB (b) films. The

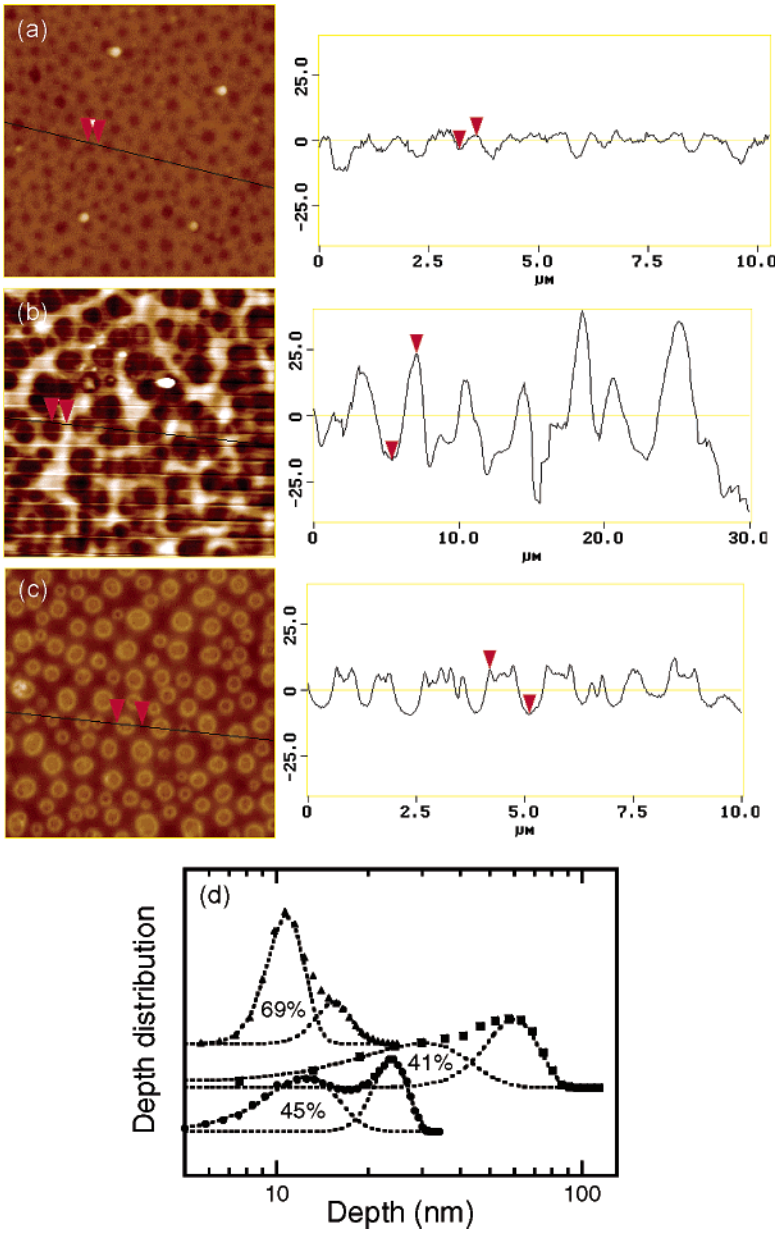

Figure 2. AFM analysis of (a) 75:25 (10 × 10 μm), (b) 50:50 (30 × 30 μm), and (c) 25:75 (10 × 10 μm) F8BT:TFB blend thin films. Topology (left) and surface line scan (right). (d) Analysis of height distribution of phases from AFM data for 75:25 (triangle), 50:50 (rectangular), and 25:75 (circle) F8BT:TFB. Fitted curves are Gaussian. The geometric phase area of the higher phase is given.

Raman spectrum of F8BT shows two strong Raman peaks at 1609 cm^{-1} (fluorene ring stretch) and 1546 cm^{-1} (benzothiadiazole ring stretch),[22,39,40] and the Raman spectrum of TFB shows two strong but partially resolved Raman peaks at 1609 cm^{-1} (fluorene ring stretch) and 1602 cm^{-1} (phenylene ring stretch).[22,39,40]

To use the Raman microscope to determine the compositions in the different domains of polymer blend thin films, it is necessary to know the relative Raman scattering cross section of each material at 633 nm excitation. For this, the Raman spectra of F8BT:TFB blends in the dilute solutions are first measured. The relative Raman intensity (I_{F8BT}/I_{TFB}) of the two materials in blend solutions is obtained based on the peak intensity at 1546 cm^{-1} (or 1609 cm^{-1}) for F8BT and the peak at 1602 cm^{-1} (or 1609 cm^{-1}) for TFB, after deconvoluting each blend solution Raman spectrum into the respective F8BT and TFB spectra. There are no changes in the peak positions and peak widths of F8BT and TFB Raman spectra with respect to their relative ratio in the blend solutions. The Raman scattering cross section is then calculated from the following equation.

$$\frac{W_{F8BT}}{W_{TFB}} = \left(\frac{I_{F8BT,X}}{\sigma_{F8BT,X}}\right) / \left(\frac{I_{TFB,Y}}{\sigma_{TFB,Y}}\right) \quad (1)$$

in which W is the weight ratio of polymer in solution. I is the Raman intensity at a given wavenumber, either X (either 1546 or 1609 cm^{-1} for F8BT) or Y (either 1602 or 1609 cm^{-1} for TFB), and σ is the Raman scattering cross section of the peak at a given wavenumber.

Figure 5a shows the relative Raman intensity vs weight ratio of F8BT:TFB in the blend solutions. On the basis of the peak either at 1546 or 1609 cm^{-1} of F8BT, we could estimate the Raman scattering cross

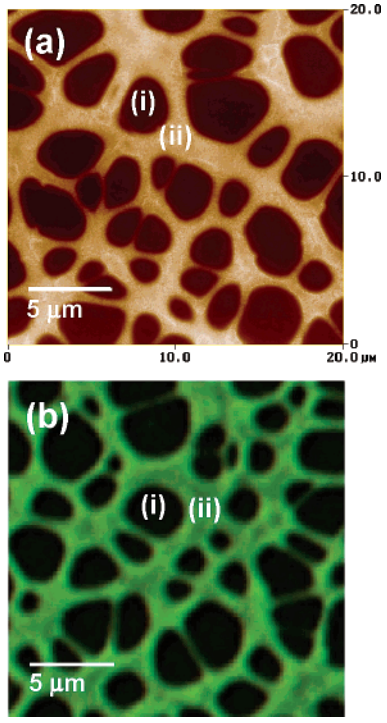

Figure 3. (a) AFM image with a 100 nm height scale (white: high region; black: low region) and (b) PL image of ∼100 nm thick F8BT:TFB (50:50) film (domain i, TFB-rich region; domain ii, F8BT-rich region). On the basis of the PL of the blend film, it is concluded that the high ridges are F8BT matrix phase (bright regions, domain ii) and the thin regions are TFB-rich enclosed phase (dark regions with very weak F8BT emission, domain i).

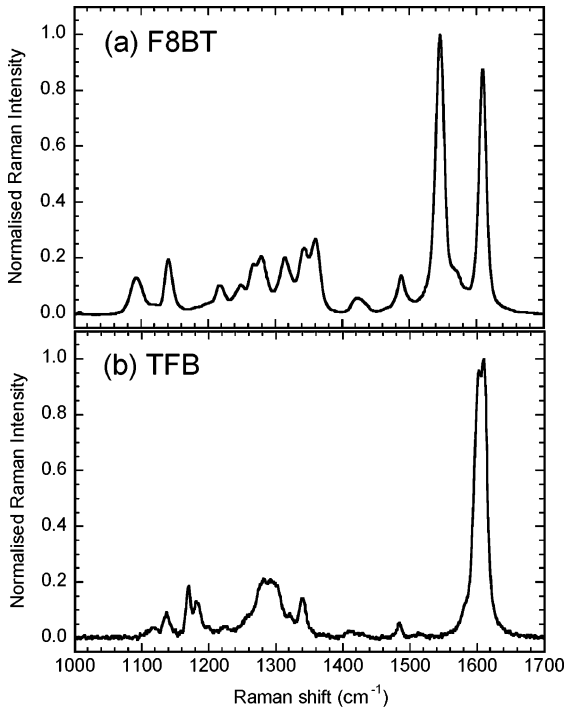

Figure 4. Normalized Raman spectrum (633 nm excitation) of ∼100 nm thick (a) F8BT and (b) TFB film on quartz substrate.

section to be about 1.8. This indicates that the F8BT will give an almost 2 times stronger Raman scattering signal than the TFB for the same weight ratio under 633 nm excitation.

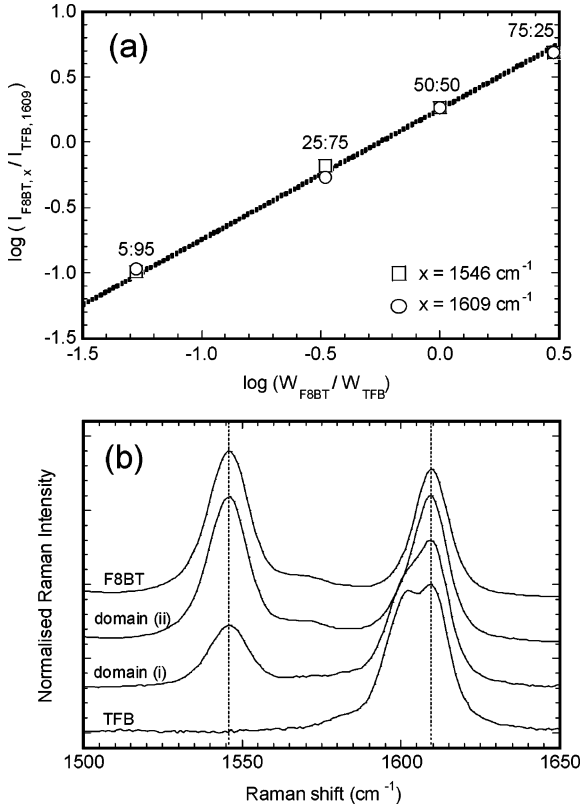

Figure 5. (a) Raman intensity vs weight ratio of F8BT:TFB in dilute solution state (log−log scale). From the intercept, the cross section of F8BT/TFB was determined to be about 1.8. (b) Raman spectra taken in two different domains of ∼100 nm thick F8BT:TFB (50:50) film (domain i, TFB-rich region; domain ii, F8BT-rich region shown in Figure 3).

$$\frac{\sigma_{\mathrm{F8BT},1546}}{\sigma_{\mathrm{TFB},1609}} \approx \frac{\sigma_{\mathrm{F8BT},1609}}{\sigma_{\mathrm{TFB},1609}} \cong 1.8 \qquad (2)$$

Figure 5b shows the Raman spectra of ∼100 nm thick F8BT:TFB (50:50) blend film taken at two different phases (domain i: TFB or TFB-rich enclosed phase; domain ii: F8BT or F8BT-rich matrix phase shown in Figure 3). By taking into account the Raman scattering cross section of these two materials, we can quantitatively assay the local composition of these blends at the micron scale in each domain. We find in this 50:50 blend film that the F8BT-rich domain has ∼65−70% F8BT and ∼30−35% TFB and that the TFB-rich domain has ∼20−25% F8BT and ∼75−80% TFB. This result confirms that in the F8BT:TFB blend system each domain is not pure at the (sub)micron length scale within each phase that appears pure to AFM images. We also notice that the TFB-rich domain includes a purer TFB (∼75−80%) than F8BT in F8BT-rich domain (∼65−70%). This may be related to the fact that in polymer blends the lower molecular weight component experiences a greater driving force to reach purer composition than the high molecular weight component. This leads for the higher molecular weight component (F8BT) to better intermix with the lower molecular weight component (TFB), yielding an impure phase.

It is important at this point to recognize that the information obtained by Raman microscopy is spatially averaged over the diffraction-limited focus spot size and averaged through the whole thickness of the polymer film weighted by the standing wave interference pattern

that is set up in the vertical direction. Therefore, it is difficult to conclude only on the basis of this result alone whether these polymer blends were intermixed at the molecular level, or the phases could actually be pure or very nearly pure but phase-separated either laterally or vertically at less than submicron length scale, or even a mixture of these two cases.

D. Vertical Phase Compositions. Core-level XPS spectra (C 1s, N 1s, and S 2p) acquired at an electron takeoff angle of 90° from the air side and from the ITO side of the F8BT:TFB polymer thin films are shown in parts a−c and d−f of Figure 6, respectively. These spectra have been normalized to the C 1s intensity.

The C 1s line shapes recorded from both sides of the films (Figure 6a,d) are eventually unchanged (fwhm = 1.3−1.4 eV) as the film composition evolves from pure F8BT to pure TFB. This is because the C 1s photoemission arises primarily from an approximately constant mix of alkyl hydrocarbon chains and phenylene aromatic cores, and the binding energy (BE) difference between these two types of carbons is small (ΔBE = 0.3 eV). As a result, the BE of the C 1s signal is a good internal reference to compensate for any surface charging or shift in sample work function to facilitate direct comparison of the other atomic core levels to extract chemical-state information.

We find several important lines of evidence for TFB enrichment at the surface and interface. First, there is a rapid attenuation of S 2p intensity with TFB dilution. The S 2p signal arises solely from the benzothiadiazole (BT) units of the F8BT polymer and is therefore a distinct marker for that polymer. The signal is split by spin−orbit coupling into S $2p_{3/2}$ and S $2p_{1/2}$ components in a 2:1 ratio separated by 1.18 eV (Figure 6c,f). The experimental BE (S $2p_{3/2}$ = 166.0 eV) is consistent with BT units where the sulfur atom bonded in the thiadiazole moiety is in a considerably less electron-withdrawing environment than in sulfonate groups (S $2p_{3/2}$ = 168.2 eV).

As the F8BT is diluted with TFB, the S 2p photoemission is rapidly attenuated even at very early stages of dilution especially from the ITO side. For example, as the F8BT weight ratio is reduced from 100% to 95% and then 75%, the intensity of S 2p normalized to C 1s from the air side (ITO side) are reduced to 79% (62%) and then 23% (11%) of their original values, all recorded at $\theta = 90°$.

We tried a similar picture using the intensity of N 1s as reference. This arises from the fact that each repeat unit of F8BT has two N atoms while TFB has one N atom. Therefore, the theoretical bulk S/N atomic ratio can be expected to decrease from 50% for the F8BT polymer to 49% for the 95% F8BT blend and then 44% for the 75% blend. Experimentally, the S/N ratio measured at air side ($\theta = 90°$) decreases from 48% to 41% and to 20% for these films, while that at the ITO side decreases even more strongly to 10% over the same range. For the middle composition ranges spanning 75% F8BT to 25% F8BT, the XPS compositions remain relatively flat, however, but still TFB enriched. Therefore, F8BT is depleted at both film−air and especially the film−substrate interface of the F8BT:TFB polymer blend films.

This is consistent further with the shift in the N 1s signal from F8BT to TFB. The TFB triarylamine nitrogen can in principle be distinguished from the BT nitrogen on account of the chemical BE shift difference

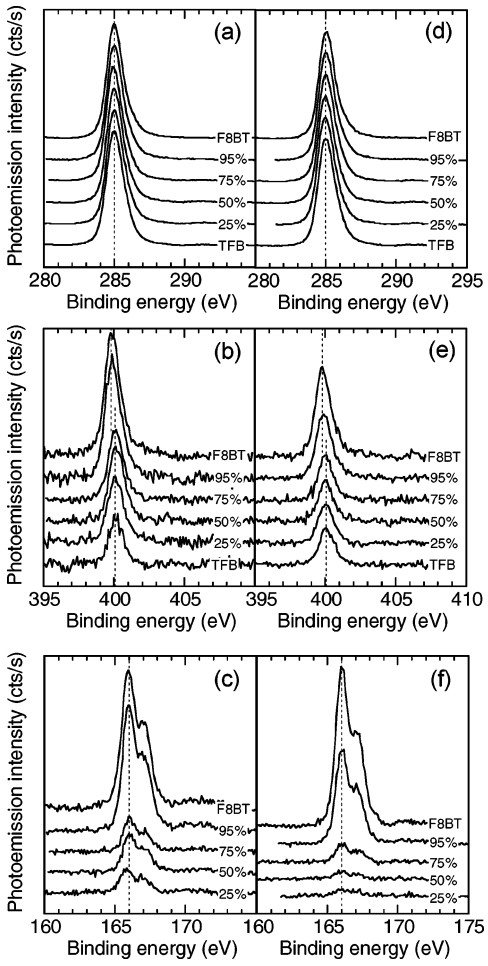

Figure 6. Core-level XPS spectra. (a) C 1s, (b) N 1s, and (c) S 2p spectra of the air side, and (d) C 1s, (e) N 1s, and (f) S 2p spectra of the ITO side of ∼90 nm thick F8BT:TFB blend films spin-coated on ITO/glass substrate. For the ITO side, the film was delaminated with carbon adhesive tape. All spectra were recorded at $\theta = 90°$ and normalized to the C 1s intensity.

(400.1 and 399.8 eV; ΔBE = 0.3 eV, vide infra). As the bulk F8BT ratio decreases from 95% to 75%, we find a distinct shift of 0.3 eV toward higher BE in the N 1s spectra for both interfaces of the film (Figure 6b,e). Therefore, the TFB units dominate photoemission from both the interfacial layers. This confirms that while the bulk composition remains F8BT-rich, the interfacial layers are already inverted to being TFB-rich. Therefore, it is clear that the TFB enriches at both the air− and ITO−substrate interfaces of these F8BT:TFB polymer blends.

The enrichment can further be quantified through an enrichment factor (χ) by taking the ratio of the weight fractions in the interfacial layer (w_{interf}) and in the bulk (w_{bulk}) according to

$$\chi = w_{TFB,interf}/w_{TFB,bulk} \tag{3}$$

The value of $w_{TFB,interf}$ is obtained from the experimental S/N ratios assuming constant physical densities for both components. The value of $w_{TFB,bulk}$ is obtained from the feed ratio. A plot of χ against $w_{TFB,bulk}$ is given in Figure 7a. The plot shows that χ is large at small values of $w_{TFB,bulk}$ but asymptotically approaches unity (as required) when $w_{TFB,bulk}$ approaches unity. Furthermore, the enrichment is more complete at the ITO

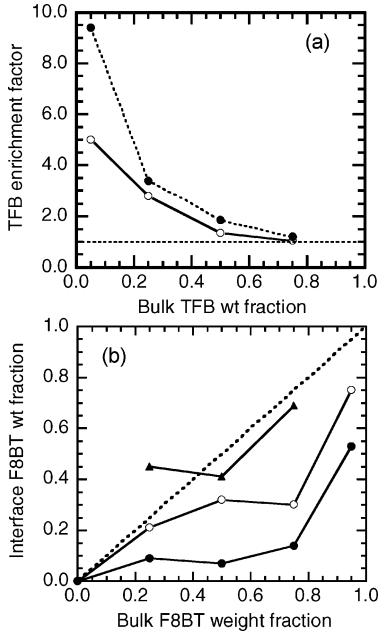

Figure 7. (a) TFB interface enrichment factor (surface/bulk TFB wt %) as a function of bulk TFB weight ratio (closed circles, ITO interface; open circles, air interface) evaluated by XPS at $\theta = 90°$. (b) Interface F8BT weight fractions evaluated by XPS against the bulk composition of F8BT:TFB films (closed circles, ITO interface; open circles, air interface). The AFM footprint (closed triangles) gives the projected phase area ratio of F8BT measured by AFM (see Figure 2d).

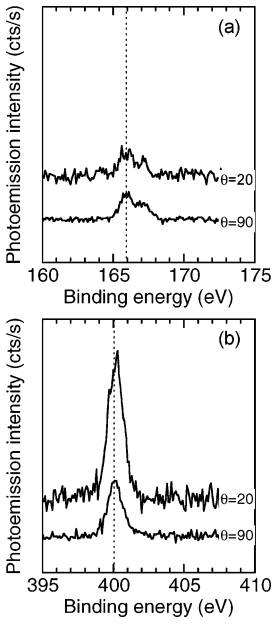

Figure 8. (a) S 2p and (b) N 1s spectra from variable photoelectron takeoff-angle experiments conducted on the ITO side of the 75:25 F8BT:TFB blend film spin-coated on ITO/glass substrate and delaminated with carbon adhesive tape. The spectra normalized to the S 2p intensity.

interface ($\chi = 9.5$ at $w_{TFB,bulk} = 0.05$) compared to the air interface ($\chi = 5.0$ at the same $w_{TFB,bulk}$). This information can alternatively be presented in terms of the F8BT weight fractions. A plot of $w_{F8BT,interf}$ against $w_{F8BT,bulk}$ is shown in Figure 7b. The convex shape of the interface weight fractions indicates depletion of F8BT at the film−air and especially the film−substrate interface region.

The enrichment of the lower surface energy component (TFB) at both air and substrate interfaces and depletion of the higher surface energy component (F8BT) from the film interfaces are consistent with thermodynamic driving force to reduce interfacial energies in the absence of strong substrate interaction. The process of solvent evaporation during spin-casting allows sufficient time for center-of-mass diffusion of these polymer chains and thus for the phase segregation to proceed to a considerable extent in the film thickness direction. Similar surface enrichment of the surfaces of polymer blends by the lower surface energy component has been characterized in numerous other (conventional) polymer blends such as polystyrene−poly(vinyl methyl ether),[41] polystyrene−polyvinylpyridine,[42] and polycarbonate−poly(dimethylsiloxane) and in other conjugated polymer blends such as polyfluorene (PFO) and F8BT.[43]

Owing to facile spinodal decomposition mechanism (i.e., an activationless process initiated by density fluctuation of the respective polymer concentrations) for the middle 50:50 compositions, phase separation of these compositions is the most advanced, and coarse features develop on relatively large length scales. The mean height difference between the F8BT-rich phase and the adjoining TFB-rich phase varies with the greatest difference observed also near the middle compositions. This is ca. 30−50 nm for a 50:50 blend film with an average thickness of ∼100 nm. As a result, morphology of the 50:50 blend has the greatest impact on quantitative XPS overlayer analysis. The severity of such complications depends, however, primarily on the mean height-to-width aspect ratio of the undulating surface features (and therefore the angular spread of local surface normals), but not on surface roughness indicators that measure mean surface deviations, such as the commonly used R_{rms}.[44]

For the blend films studied here, the lateral size of the surface structures is large (0.1−5 μm wide) while the vertical variation is relatively small (typically less than a few tens of nanometers). Therefore, the aspect ratio of these structures is modest (less than 0.01), and the angular dispersion of local surface normals about the mean is also small (typically less than ±5°, although excursions beyond ±20° can be found over small fractions of the surface area). Overall, this average dispersion is sufficiently small to be neglected in variable-angle spectroscopy.[44]

Variable photoelectron takeoff-angle experiments were conducted on the ITO side of the 75% F8BT blend film. The data normalized to the S 2p intensity are presented in Figure 8. The ITO side of the polymer film is smooth, and the data can therefore be interpreted in a straightforward manner using a molecular-scale surface enrichment factor defined relative to F8BT ($\zeta_{TFB/F8BT,20°}$):

$$\zeta_{TFB/F8BT,20°} = (N/S)_{\theta=20°}/(N/S)_{\theta=90°} \quad (4)$$

In this way we obtained $\zeta_{TFB/F8BT,20°} = 2.2$, which is well above the factor of unity for uniform depth distribution of the two polymers. This molecular enrichment factor can be related to the mean decay length (d_{xps}) of the ratio of the two polymer concentrations from the surface using the following overlayer equation:

$$\zeta_\theta = [1 - \exp(-d_{xps}/\lambda_0 \sin\theta)]/[1 - \exp(-d_{xps}/\lambda_0)] \quad (5)$$

with $\lambda_0 = 25$ Å and $\theta = 20°$. We find $d_{xps} = 6-10$ Å for TFB relative to F8BT. This result complements the θ

Table 2. Surface Atomic Stoichiometries (N/S) at the Two Photoelectron Take-Off Angles (θ) and Molecular Surface Enrichment Factor ($\zeta_{TFB/F8BT,20°}$) for F8BT:TFB Polymer Blend Thin Films[a]

	$(N/S)_{bulk}$	A_{F8BT}	w_{F8BT}	$(N/S)_{\theta=90}$	$(N/S)_{\theta=20}$	$\zeta_{TFB/F8BT,20°}$
film−air interface						
100:0 F8BT:TFB	2.0	1.0	1.0	2.1	1.9	0.9
95:05 F8BT:TFB	2.05		0.75	2.45	2.25	0.9
75:25 F8BT:TFB	2.25	0.7	0.3	5.1	10	2.0
50:50 F8BT:TFB	2.7	0.4	0.3	4.8	4.7	1.0
25:75 F8BT:TFB	4.2	0.45	0.2	6.8	6.9	1.0
substrate−film interface						
75:25 F8BT:TFB	2.25		0.15	10.5	23	2.2

[a] The bulk $(N/S)_{bulk}$ values are deduced from the feed ratio. A_{TFB} is the TFB "footprint" determined from the projected area ratio of the lower-lying TFB phase to the total area sampled by AFM. w_{F8BT} is the effective surface composition of F8BT in the surface region of the films evaluated by XPS at $\theta = 90°$.

$= 90°$ composition-dependent trend (see Figure 7b) to confirm the molecular-scale segregation of TFB to the substrate interface. The greater propensity for TFB to form a molecular "wetting layer" at the film−substrate interface may be related to the solvent concentration gradient across the film thickness in the dry-down stage. This facilitates greater polymer segment mobility at the film−substrate interface compared to the film−air surface. Compositions that are even richer in TFB cannot be readily analyzed at $\theta = 20°$ because of the far weaker S 2p signal.

Since the film−air interface exhibits a diverse range of morphological structures, variable-angle experiments were performed on a range of compositions. The data collected from the air side of these films are put together in Table 2.

For the pure F8BT film, the surface N/S atomic concentration is very near the idealized value of 2. For the 95:5 F8BT:TFB film, there is a definite excess of TFB on the surface vs the bulk. $(N/S)_{\theta=90°} = 2.45$; cf. $(N/S)_{bulk} = 2.05$. However, the molecular surface enrichment factor ($\zeta_{TFB/F8BT,20°}$) determined by variable-angle experiments is near unity. This indicates that the excess TFB on the surface is not molecularly thin; thus, it probably exists as isolated pockets over the primary F8BT-rich phases.

For the 75:25 blend, however, there is both a surface excess of TFB and a marked molecular enrichment by TFB from the $(N/S)_{\theta=90°}$ and $(N/S)_{\theta=20°}$ data. For the blends that are even richer in TFB (both the 50:50 and 25:75 compositions), the XPS data indicate a surface excess of TFB, but no surface segregation at the molecular level was detected since the composition is largely independent of photoemission angle. We believe that the lack of photoemission angle dependence is not due to increased surface roughness but that the film−air surface phase behavior of these F8BT−TFB films are dominated by bulk-scale demixing effects rather than molecular-scale enrichment. For example, for the 25:75 F8BT:TFB composition, the phase area ratio (A_{F8BT}) as determined by AFM using height histograms is 45%, but the weight fraction of F8BT in the topmost 50 Å is apparently constant at 20%. This might indicate that the TFB-rich phase is discontinuous at the surface—about half of the primary F8BT-rich phases are eclipsed by TFB-rich domains. The thickness of such domains appears to be greater than 50 Å, and so they are molecularly thick but still *very thin* compared to the film thickness. This finding is consistent with fluorescence microscope images which show substantially uniform fluorescence from the primary F8BT-rich phases (made possible by the short absorption path length through the TFB-rich caps).

The picture that emerges thus for the film−air interface is that the exposed F8BT primary phases in the middle and slightly TFB-rich compositions are partially covered by secondary TFB-rich domains. These secondary domains do not extend laterally to form a continuous "wetting layer" as found at the film−substrate interface. Furthermore, the size of these domains is rather small (but thicker than 50 Å) since they do not readily show up in tapping-mode AFM (i.e., they do not sufficiently affect the viscoelastic response of the polymer film within the Hertzian deformation region sensed by the probe). Hence, we consider that these domains are in the form of discontinuous "islands" or "caps" over F8BT-rich phases, formed in a bulklike demixing process.

In summary of this section, the XPS data suggest that only 20−30% of the exposed film−air surface of the interesting middle compositions (75:25−25:75) is F8BT. The rest of it is the TFB distributed between the two primary phases. The film−substrate interface, on the other hand, is almost completely wetted (>90%) by a TFB layer, which incidentally turns out to be very favorable to mediate hole injection into the F8BT.

E. Thin-Film Formation Model. Using the information obtained from the blend solution phase diagram, morphological and lateral and vertical compositional analysis of the F8BT:TFB blend thin films described in section IIIA−D, we propose a simple model for the formation of the polymer blend thin film during spin-casting (Figure 9).

First, the polymer solution is dispensed onto the substrate, typically at a concentration of 1.0−2.0% w/v (10−20 mg/mL). For a 1% solution, to achieve a final dry film thickness of 100 nm, the initial wet film thickness is then 10 μm. As the substrate starts to spin, liquid flow spreads the solution over the substrate to the edges (step 1). At the end of this spin-up stage, the wet film thickness for a typical 1% polymer solution is thinned down to about 10 μm by centrifugal effects.

As the solvent continues to evaporate, according to the phase diagram (Figure 1), the F8BT-rich + solvent regions will phase separate at low solids contents. For blends that are near 50:50 in F8BT:TFB composition, this is likely to be a process initiated by density fluctuation of the respective polymer concentrations (i.e., spinodal decomposition). On the other hand, biblend compositions that are strongly enriched in one or the other polymer will likely show nucleation driven behavior during the phase separation. As solvent evaporation progresses there is a rapid increase in the solution concentration (step 2).

As more solvent evaporates, the phases continue to expel "guest" polymer material. Some of this material

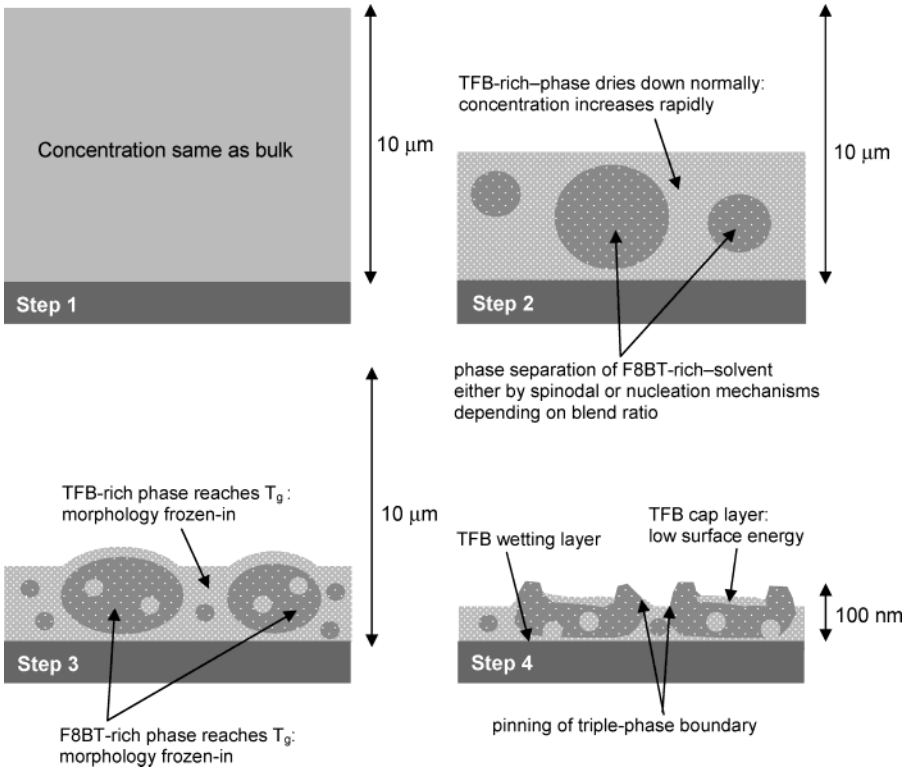

Figure 9. Proposed model for the development of the thin-film phase-separated structure in F8BT:TFB blends during spin-coating process: spin-off (step 1), solvent evaporation (step 2), morphology frozen-in (step 3), and thin-film formation (step 4).

does, however, become entrapped as separate domains inside larger domains of the other phase until the system reaches the glass transition temperature which results in a "freezing" of the morphological structure. In other words, as the solvent evaporates during the spin-coating process, the T_g of the mixture rises, until it reaches room temperature, at which point polymer chain motions cease and the structure existing at that time is "frozen". The T_g of the F8BT-rich phase reaches room temperature, and the morphology is frozen in. Subsequently, the TFB-rich regions are also frozen; however, solvent evaporation continues for both phases (step 3). Further solvent evaporation continues after this time; however, there is no more microscopic development of the phase-separated morphologies already formed. Additional to the glass transition effect, there is the inherent chemical solubility effect of the solvent, which also plays a part in the phase and morphology formation. Temperature is crucial in this process—several degrees change can result in different solution separation and a different phase arrest point during spin-casting.

The final film structure (step 4), in particular for low F8BT content blends, consists of a volcano-like surface morphology, presumed to be the result of pinning of the triple-phase boundary between the F8BT-rich, TFB-rich, and air phases. This is similar to the effects seen in the drying of coffee stains and in ink-jet-printed polymers, where the solute diffuses to the edge of the drying drop. XPS data indicate the existence of a TFB wetting layer at the substrate interface and a TFB capping layer at the air interface.

F. LED Characteristics. Further knowledge of the polymer blend film structure enables the proposition of a model for LED operation. The TFB wetting layer might act as a hole-accepting/transporting and electron-blocking layer at the anode interface, while the TFB capping layer probably acts to block electron injection in certain areas at the cathode, confining efficient injection. This then may produce a high degree of spatial confinement of charge carriers, which will lead to high recombination efficiency.

Work to examine LEDs without an additional hole-injection/transporting layer such as PEDT:PSS, since TFB (hole-accepting/transporting polymer) is already present at the anode interface, has been performed. The current−voltage ($I-V$) and efficiency−voltage ($\eta-V$) characteristics of F8BT:TFB LEDs with/without a PEDT:PSS layer are plotted in Figure 10. Devices with PEDT:PSS show well-behaved $J-V$ and $\eta-V$ characteristics. They exhibit a sharp turn-on in both current (threshold of 1 μA/cm^2) and luminance (threshold of 1 mcd/m^2) at ∼1.9 V, which is close to band-edge offsets between the conduction and valence bands of F8BT and TFB, similar to a "type II" heterojunction with minimum semiconductor gap between the valence band edge for the hole-transport polymer and the conduction band edge for the electron-transport polymer (see Figure 10a, inset). Such a low-voltage operation is characterized by a barrier-free electron−hole capture process across this heterojunction to form a bound interface state.[20] These devices show extremely low levels of leakage currents of the order of 10 nA/cm^2 at 1.0 V below turn-on. This may be related to the role of PEDT:PSS acting as a blocking layer against indium and oxygen diffusion from ITO anode into the emissive polymer layer.[45] The maximum EL photometric efficiency of these devices is 13 cd/A, giving a power efficiency of 18 lm/W (at 0.8 mA/cm^2, 2.2 V) immediately after the onset of bipolar injection.

On the other hand, the devices fabricated without PEDT:PSS also show well-behaved $J-V$ and $\eta-V$ characteristics with a sharp turn-on in both current (threshold of 1 μA/cm^2) and luminance (threshold of 1 mcd/m^2) at ∼1.9 V, which is the same value as observed

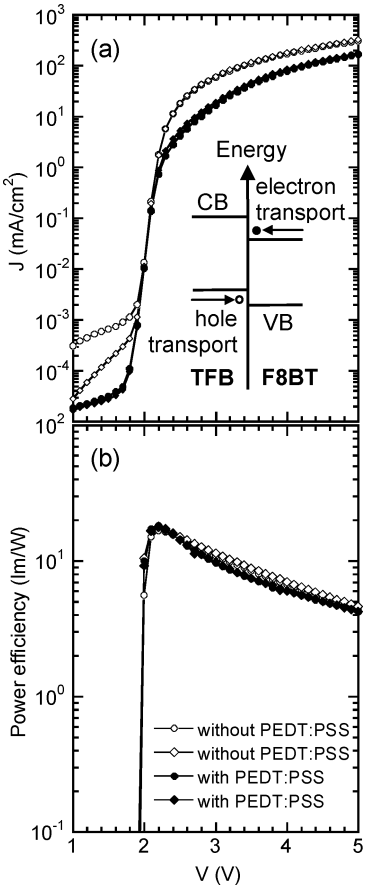

Figure 10. (a) Current−voltage and (b) power efficiency−voltage characteristics of the encapsulated ITO/F8BT:TFB blend (50:50, 80 nm)/Ca (5 nm)/Al (400 nm) LEDs with/without a PEDT:PSS (60 nm) layer (two of each). Inset: scheme for heterojunction formed between F8BT and TFB. Energies for the top of the valence band (VB) with respect to the vacuum level, estimated from cyclic voltammetry, are 5.33 eV (TFB) and 5.89 eV (F8BT). Electrons from F8BT and holes from TFB are transported, and exciton formation results from electron−hole capture at the heterojunction. F8BT is a high electron mobility polymer, and TFB is a high hole mobility polymer.

in the devices with PEDT:PSS. This indicates that removing the PEDT:PSS layer does not increase the energy barriers for hole injection from ITO to TFB and electron−hole recombination at the TFB and F8BT interfaces, as expected from a similar ionization potential of TFB (∼5.33 eV) as PEDT:PSS (∼5.30 eV).[46] This confirms good hole injection and transport properties of TFB. These devices yield a current density about 2−4 times larger than that of the PEDT:PSS devices, with significant levels of low-voltage leakage current. However, the maximum EL photometric efficiency observed in these devices is as high as the devices with an additional PEDT:PSS layer, which is 12−13 cd/A with a power efficiency of 17−18 lm/W (at 1.7 mA/cm^2, 2.2 V). Even slightly higher initial photometric and power efficiencies are measured above 2 V compared to the PEDT:PSS devices. These devices also show considerable structures in PL and EL emission at the micron length scale originated from a phase separation of F8BT:TFB polymers in their blend, as observed in the PEDT:PSS devices.

These results show clearly that initial performance equivalent to the devices with a PEDT:PSS layer is achievable in LEDs which contain only a single layer of F8BT:TFB polymer blend material, confirming that the TFB wetting layer at the ITO anode interface induced by the self-organized vertical phase separation in this blend thin film acts efficiently as a hole-accepting/transporting layer.

IV. Conclusion

In this report, we have discussed some of the factors that affect the final morphology of conjugated polymer blend thin films and presented detailed studies on the thin-film morphology of the blends, in particular focusing on the lateral and vertical phase compositions and structures. The thin-film morphologies of F8BT:TFB blends produced by spin-casting show distinctive micron-scale lateral phase separations. However, these phase-separated domains are not pure at the submicron length scale, and a nanoscale vertical phase segregation occurs in these thin blend films, with enrichment of the lower surface energy component (TFB) at both air and substrate interfaces. Imaging of the spatial uniformity of electroluminescence emission on the microscopic scale indicates spatially localized charge carrier recombination in LEDs fabricated with these blends. On the basis of these experimental results, we have proposed a simple model for the formation of the F8BT:TFB blend thin films which may play an important role in operation of blend LEDs. Work to examine LEDs without an additional hole-injection/transporting layer such as a PEDT:PSS, since TFB wetting layer (hole-transporting polymer) is already present at the anode interface, has been performed, and the results show that initial performance equivalent to devices with a PEDT:PSS layer is achievable in LEDs which contain only a single layer of F8BT:TFB polymer blend.

Acknowledgment. The XPS measurements have been performed at the surface science laboratory at National University of Singapore (NUS) or CLRC (Daresbury Laboratory). We acknowledge Mr. Wong (NUS) and Dr. G. Beamson (Daresbury) for their help in XPS measurements.

References and Notes

(1) Burroughes, J. H.; Bradley, D. D. C.; Brown, A. R.; Marks, R. N.; Mackay, K.; Friend, R. H.; Burn, P. L.; Holmes, A. B. *Nature (London)* **1990**, *347*, 539.
(2) Friend, R. H.; Gymer, R. W.; Homes, A. B.; Burroughes, J. H.; Marks, R. N.; Taliani, C.; Bradley, D. D. C.; Santos, D. A. D.; Brédas, J. L.; Lögdlund, M.; Salaneck, W. R. *Nature (London)* **1999**, *397*, 121.
(3) Cao, Y.; Parker, I. D.; Yu, G.; Zhang, C.; Heeger, A. J. *Nature (London)* **1999**, *397*, 414.
(4) Kim, J. S.; Granström, M.; Friend, R. H.; Johansson, N.; Salaneck, W. R.; Daik, R.; Feast, W. J.; Cacialli, F. *J. Appl. Phys.* **1998**, *84*, 6859.
(5) Kim, J. S.; Friend, R. H.; Cacialli, F. *Appl. Phys. Lett.* **1999**, *74*, 3084.
(6) Parker, I. D.; Cao, Y.; Yang, C. Y. *J. Appl. Phys.* **1999**, *85*, 2441.
(7) Millard, I. S. *Synth. Met.* **2000**, *111*, 119; see also http://www.cdtltd.co.uk.
(8) Burrows, P. E.; Forrest, S. R.; Zhou, T. X.; Michalski, L. *Appl. Phys. Lett.* **2000**, *76*, 2493.
(9) Bernius, M. T.; Inbasekaran, M.; O'Brien, J.; Wu, W. S. *Adv. Mater.* **2000**, *12*, 1737.
(10) Yu, G.; Gao, J.; Hummelen, J. C.; Wudl, F.; Heeger, A. J. *Science* **1995**, *270*, 1789.
(11) Halls, J. J. M.; Walsh, C. A.; Greenham, N. C.; Marseglia, E. A.; Friend, R. H.; Moratti, S. C.; Holmes, A. B. *Nature (London)* **1995**, *376*, 498.
(12) Halls, J. J. M.; Arias, A. C.; MacKenzie, J. D.; Inbasekaran, M.; Woo, E. P.; Friend, R. H. *Adv. Mater.* **2000**, *12*, 498.

(13) Wilkinson, C. I.; Lidzey, D. G.; Palilis, L. C.; Fletcher, R. B.; Martin, S. J.; Wang, X. H.; Bradley, D. D. C. *Appl. Phys. Lett.* **2001**, *79*, 171.
(14) Morgado, J.; Moons, E.; Friend, R. H.; Cacialli, F. *Adv. Mater.* **2001**, *13*, 810.
(15) Morgado, J.; Friend, R. H.; Cacialli, F. *Appl. Phys. Lett.* **2002**, *80*, 2436.
(16) Arias, A. C.; Corcoran, N.; Banach, M.; Friend, R. H.; MacKenzie, J. D.; Huck, W. T. S. *Appl. Phys. Lett.* **2002**, *80*, 1695.
(17) Snaith, H. J.; Arias, A. C.; Morteani, A. C.; Silva, C.; Friend, R. H. *Nano Lett.* **2002**, *2*, 1353.
(18) Moons, E. *J. Phys.: Condens. Matter* **2002**, *14*, 12235.
(19) Corcoran, N.; Arias, A. C.; Kim, J. S.; MacKenzie, J. D.; Friend, R. H. *Appl. Phys. Lett.* **2003**, *82*, 299−301.
(20) Morteani, A. C.; Dhoot, A. S.; Kim, J. S.; Silva, C.; Greenham, N. C.; Friend, R. H.; Murphy, C.; Moons, E.; Cina, S.; Burroughes, J. *Adv. Mater.* **2003**, *15*, 1708.
(21) Cina, S.; Baynes, N.; Moons, E.; Friend, R. H.; Burroughes, J.; Towns, C.; Heeks, K.; O'Dell, R.; O'Connor, S.; Athanassopoulou, N. *P. Soc. Photo-Opt. Ins. (SPIE)* **2001**, *4279*, 221.
(22) Kim, J. S.; Ho, P. K. H.; Murphy, C. E.; Baynes, N.; Friend, R. H. *Adv. Mater.* **2002**, *14*, 206.
(23) Meyerhofer, D. *J. Appl. Phys.* **1978**, *49*, 3993.
(24) Lawrence, C. J. *Phys. Fluids* **1988**, *31*, 2786.
(25) Bates, F. S. *Science* **1991**, *251*, 898.
(26) Tanaka, K.; Takahara, A.; Kajiyama, T. *Macromolecules* **1996**, *29*, 3232.
(27) Walheim, S.; Schaffer, E.; Mylnek, J.; Steiner, U. *Science* **1999**, *283*, 520.
(28) Jones, R. A. L.; Richards, R. W. *Polymers at Surfaces and Interfaces*; Cambridge University Press: Cambridge, 1999.
(29) Boltau, M.; Walheim, S.; Mlynek, J.; Krausch, G.; Steiner, U. *Nature (London)* **1998**, *391*, 877.
(30) Campbell, A. J.; Bradley, D. D. C.; Antoniadis, H. *Appl. Phys. Lett.* **2001**, *79*, 2133.
(31) Herguth, P.; Jiang, X.; Liu, M. S.; Jen, A. K.-Y. *Macromolecules* **2002**, *35*, 6094.
(32) Redeker, M.; Bradley, D. D. C.; Inbasekaran, M.; Wu, W. W.; Woo, E. P. *Adv. Mater.* **1999**, *11*, 241.
(33) Beamson, G.; Briggs, D. *High Resolution XPS of Organic Polymers: The Scienta ESCA300 Database*; John Wiley & Sons: West Sussex, UK, 1992.
(34) Van Krevelen, D. W. *Properties of Polymers: Their Correlation with Chemical Structure; Their Numerical Estimation and Prediction from Additive Group Contributions;* Elsevier: Amsterdam, 1990.
(35) Stevenson, R.; Arias, A. C.; Ramsdale, C.; MacKenzie, J. D.; Richards, D. *Appl. Phys. Lett.* **2001**, *79*, 2178−2180.
(36) Kim, J. S.; Ho, P. K. H.; Murphy, C. E.; Seeley, A. J. A. B.; Grizzi, I.; Burroughes, J. H.; Friend, R. H. *Chem. Phys. Lett.* **2004**, *386*, 2.
(37) Tian, B.; Zerbi, G.; Schenk, R.; Müllen, K. *J. Chem. Phys.* **1991**, *95*, 3191.
(38) Casado, J.; Puig, J. J. M.; Hernandez, V.; Zotti, G.; Navarrete, J. T. L. *J. Phys. Chem. A* **2000**, *104*, 10656.
(39) Ariu, M.; Lidzey, D. G.; Bradley, D. D. C. *Synth. Met.* **2000**, *111−112*, 607.
(40) Colthup, N. B.; Daly, L. H.; Wiberley, S. E. *Introduction to Infrared and Raman Spectroscopy*, 3rd ed.; Academic Press: San Diego, 1990.
(41) Pan, D. H. K.; Prest, W. M., Jr. *J. Appl. Phys.* **1985**, *58*, 2861.
(42) Kang, H.; Lee, S.-H.; Kim, S. C.; Char, K. H. *Macromolecules* **2003**, *36*, 8579.
(43) Chappell, J.; Lidzey, D. G.; Jukes, P. C.; Higgins, A. M.; Thompson, R. L.; O'Connor, S.; Grizzi, I.; Fletcher, R.; O'Brien, J.; Geoghegan, M.; Jones, R. A. L. *Nature Mater.* **2003**, *2*, 616.
(44) Fadley, C. S.; Baird, R. J.; Siekhaus, W.; Novakov, T.; Bergstrom, S. A. L. *J. Electron. Spectrosc. Relat. Phenom.* **1974**, *4*, 93.
(45) Fahlman, M.; Salaneck, W. R. *Surf. Sci.* **2002**, *500*, 904.
(46) Brown, T. M.; Kim, J. S.; Friend, R. H.; Cacialli, F.; Daik, R.; Feast, W. J. *Appl. Phys. Lett.* **1999**, *75*, 1679.

MA035750I